

Article

Texture and Geochemistry of Scheelites in the Tongshankou Deposit in Daye, Hubei, China: Implication for REE Substitution Mechanism and Multistage W Mineralization Processes

Rui-Zhe Zhao ^{1,2}, Min-Fang Wang ^{1,*}, Huan Li ³ , Xiao-Yu Shang ¹, Zaheen Ullah ^{3,4}  and Jun-Peng Wang ⁵

¹ School of Earth Resources, China University of Geosciences, Wuhan 430074, China; rz1222310@cug.edu.cn (R.-Z.Z.); ShangXY@cug.edu.cn (X.-Y.S.)

² Hainan Key Laboratory of Marine Geological Resources and Environment, Hainan Marine Geology Survey, Haikou 570000, China

³ Key Laboratory of Metallogenic Prediction of Nonferrous Metals and Geological Environment Monitoring, Ministry of Education, School of Geosciences and Info-Physics, Central South University, Changsha 410083, China; lihuan@csu.edu.cn (H.L.); zaheengeo@gmail.com (Z.U.)

⁴ Department of Geology, University of Baltistan Skardu, Skardu 16100, Pakistan

⁵ School of Earth Sciences, China University of Geosciences, Wuhan 430074, China; wangjp@cug.edu.cn

* Correspondence: wangmingfang@cug.edu.cn



Citation: Zhao, R.-Z.; Wang, M.-F.; Li, H.; Shang, X.-Y.; Ullah, Z.; Wang, J.-P. Texture and Geochemistry of Scheelites in the Tongshankou Deposit in Daye, Hubei, China: Implication for REE Substitution Mechanism and Multistage W Mineralization Processes. *Minerals* **2021**, *11*, 984. <https://doi.org/10.3390/min11090984>

Academic Editor: Maria Boni

Received: 28 July 2021

Accepted: 7 September 2021

Published: 9 September 2021

Publisher's Note: MDPI stays neutral with regard to jurisdictional claims in published maps and institutional affiliations.



Copyright: © 2021 by the authors. Licensee MDPI, Basel, Switzerland. This article is an open access article distributed under the terms and conditions of the Creative Commons Attribution (CC BY) license (<https://creativecommons.org/licenses/by/4.0/>).

Abstract: The Tongshankou skarn deposit in the Edong ore district is a typical metasomatic deposit associated with adjacent granodiorite porphyry and carbonate rocks. Using comprehensive microscopic observations, mineralogical and geochemical analysis, scheelite grains in the skarns can be classified into three major types, showing multi-stage mineralization characteristics. In the redox fluid environment, scheelites that occur with garnets usually have affinity to garnets, while in later skarn phases others exist with oxides and sulfides. They can be subdivided by trace elements, such as Nb and Eu, to discuss the detailed ore-forming process. Scheelites have three typical substitution mechanisms including: $2\text{Ca}^{2+} \rightleftharpoons \text{REE}^{3+} + \text{Na}^{+}$ (1); $\text{Ca}^{2+} + \text{W}^{6+} \rightleftharpoons \text{REE}^{3+} + \text{Nb}^{5+}$ (2); and $3\text{Ca}^{2+} \rightleftharpoons 2\text{REE}^{3+} + \square\text{Ca}$ ($\square\text{Ca}$ = Ca site vacancy) (3). Plagioclase or various hydrothermal stages can cause Eu anomalies to fluctuate from positive to negative, and these processes can cause particular zonation in W and Mo contents in scheelites. This study highlights the use of texture and geochemistry of scheelites in skarn deposits, depicting the W mineralization processes.

Keywords: scheelite; CL imaging; geochemistry; skarn; double linear grain; Tongshankou

1. Introduction

Tungsten has been listed as one of the most important industrial metals in alloy manufacturing, with a wide range of applications, and has also been listed as one of the critical metals by nearly all developed countries due to its strategic importance [1]. The Edong ore district, located in the Middle–Lower Yangtze River belt (MLYRB), is a multi-metal metallogenic belt containing mostly porphyry and skarn type deposits. The ore district includes the Tongshankou porphyry-skarn Cu-Mo-(W) deposit, and has a comparable geological environment to the adjacent Ruanjiawan and Fujiashan-Longjiaoshan W deposits [2–4]. Scheelite is the main tungsten mineral in both the porphyry and skarn systems in the Tongshankou area. There has been, however, no comprehensive study on the genesis of scheelites and the W transportation mechanism in the Tongshankou deposits. A cold cathodoluminescence study revealed pores and inner texture in scheelite, indicating multi-stage ore formation [5]. Tungsten is mostly concentrated in mafic enclaves compared to diorite intrusions and limestone stratum, which may have originated from a different magma source due to mantle upwelling [6]. The focus of this research is to describe the

field investigation, geological relationship, textural mineralogy and geochemistry of scheelites in a skarn system in the Tongshankou deposit, for better understanding of their REE substitution mechanisms and formation processes of scheelite. In addition, this research provides insight into the ore prospecting based on the ore-forming processes and geochemical characteristics. The purpose of this research is to investigate the tungsten metallogenic process in order to illustrate the genesis of scheelite mineralization in Tongshankou deposit.

2. Regional and Deposit Geology

The MLYRB is one of the most important polymetallic mineralization belts of the Yangtze plate. The Lower Yangtze depression is dominated by sedimentary cap rocks in the north of Yangtze plate, and Dabie orogenic belt in the south [7,8] (Figure 1a). The region is bounded by the Xiangfan–Guangji fault to the northwest, the Tancheng–Lujiang regional strike–slip fault to the northeast and the Yangxin–Changzhou fault to the south [9] (Figure 1b). From Echeng to Yinzu intrusions, a significant number of north-dipping thrust faults are linked together, forming complicated tectonics, thrust folds that controlled the majority of mineralized structures in this area, including Tongshankou and Daye [10]. The Yanshanian and Himalayan orogeny in Mesozoic time caused the main magmatic intrusions in the Edong district, and played the major role of orogeny, which is directly connected with Yinzu and Lingxiang intrusions. Echeng, Tieshan, Jinshandian, Yinzu, Lingxiang and Yangxin are the six main magmatic intrusions exposed in the close vicinity of the study area (Figure 2). The Daye syncline and Yinzu anticline, which exist between the Yinzu and Lingxiang intrusions, are key structures that influenced the metallogeny of the Tongshankou region. At 143–145 Ma, the early formed porphyry system was an oxidation type Cu (Mo) deposit [11] that played the role of intermediate-acid intrusion rocks in skarn mineralization. As mentioned, complicated tectonics within this area included seven composite folds: Echeng anticline, Huajiahu syncline, Tieshan anticline, Huangjinshan syncline, Baoan–Wangren anticline, Daye syncline and Yinzu anticline, most of which were formed during early Yanshanian. There are over 200 faults within the Edong district with different trending that can be classified relatively into 5 types: NWW, NE, NNE, NW and E–W [9–12].

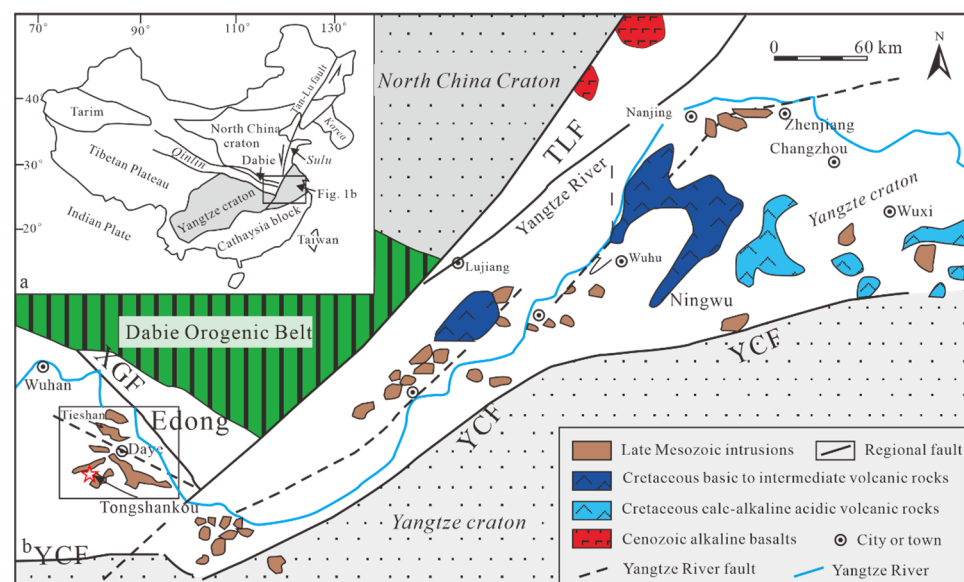


Figure 1. (a) Simplified geologic map of the Middle–Lower Yangtze River belt (MLYRB), modified after [9–13]. Abbreviations: TLF–Tancheng–Lujiang Fault, XGF–Xiangfan–Guangji Fault, YCF–Changzhou–Yangxin Fault; (b) detail location of the Edong ore district and simple illustration of surrounding geology environment (modified after [9,12,13]).

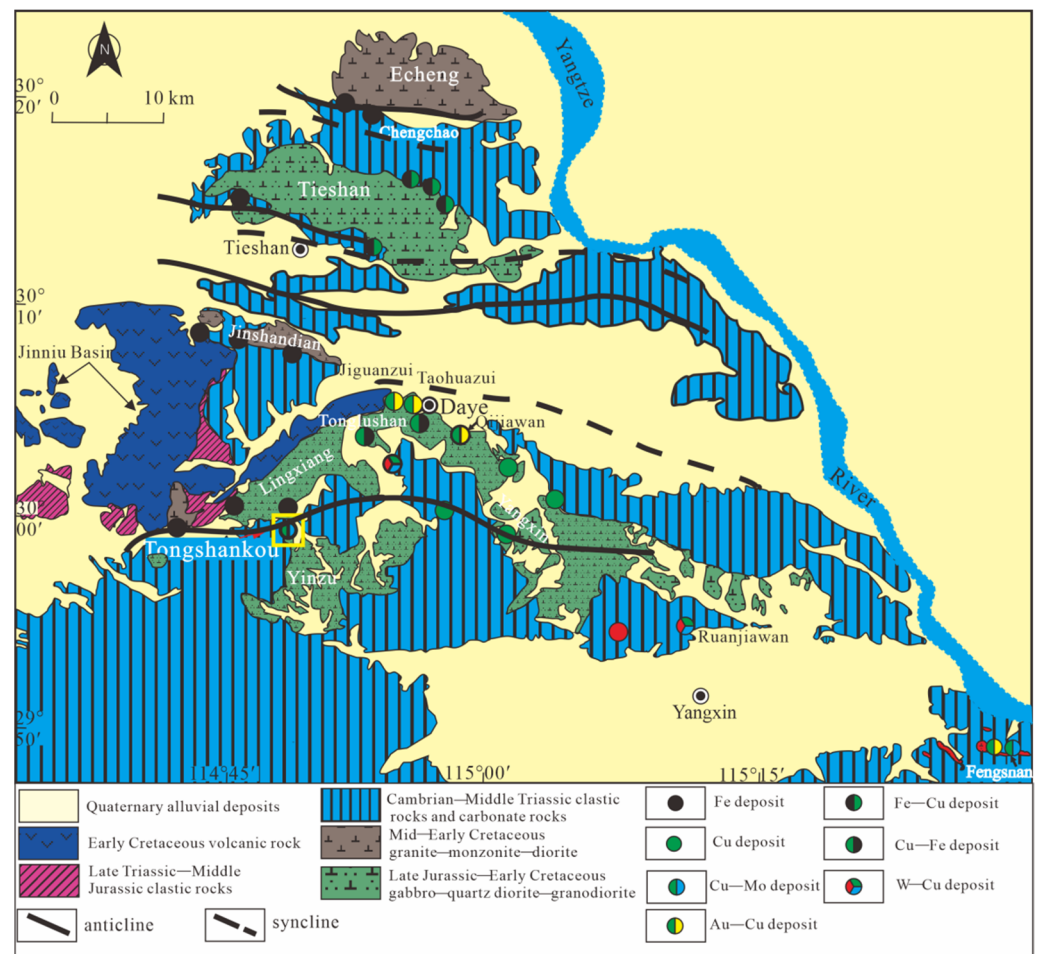


Figure 2. The Edong ore district geologic map, illustrating the main magmatic intrusions in this area (modified after [13]).

The nearby Early Triassic carbonate rocks strata offered a suitable geochemical environment for Ca-skarn formation. K-feldspar, biotite, garnet, apatite, wollastonite, diopside, chlorite, hornblende, quartz, scheelite, pyrite, molybdenite, chalcopyrite, calcite and galena are the most common skarn minerals. Scheelite is a common mineral associated with garnet, oxides, sulfides and quartz in skarn deposits [14]. There is a zonation of intensive skarn alteration, weak skarn alteration and mild chlorite alteration within the deposit district from intrusions to the carbonate strata [15].

According to previous Sr-Nd and U-Pb zircon studies, the Tongshankou deposits were formed around 145 Ma and are linked to skarn mineralization [12]. The Tongshankou skarn deposit is a typical metasomatic deposit with layers of granodiorite porphyry and carbonate rocks. The Edong ore district, which is part of the largest MLYRB deposits, has multi-metal resources such as Cu, Fe, Ni, Au, W, Mo, Mn, Pb, Zn and Co. The Tongshankou deposit has an association of economically Cu-Mo-W (Au) ore bodies that have been prospected, mostly in the porphyry portions that are localized towards endoskarn rocks [7,8] (Figure 3).

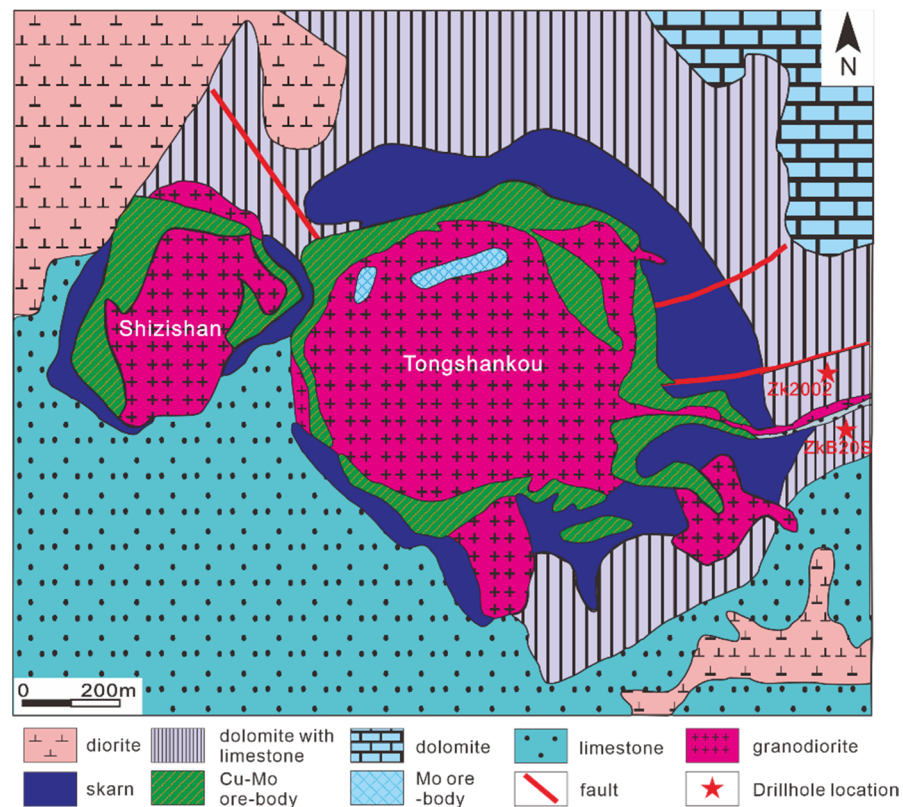


Figure 3. Geologic map of the Tongshankou deposit (simplified from [9]).

3. Sample and Analytical Methods

3.1. Sample Description

Representative rock and ore samples were collected from two drill holes in the Tongshankou deposit to determine mineral composition and scheelite trace element geochemistry. Exoskarn samples were collected from molybdenite and scheelite-garnet zone (ZK2002-1) at a depth of 760 m, and from the ore-bearing quartz-sulfides zone (ZK2002-2) at a depth of 1250 m, while the endoskarn samples of diopside-garnet (ZKB20S) were taken at a depth of 650–700 m.

Scheelites in the Tongshankou deposit are widely distributed in both endoskarn and exoskarn, and are associated with garnet. Three types of scheelite (SchA, B and C) are identified under the microscope on the basis of its paragenesis. Epidote, chlorite, actinolite and serpentine are the most common retrograde minerals here, which formed after skarn stage. SchA is subhedral to anhedral scheelite within the ZK2002 exoskarn sample. Some grains of SchA are associated with sulfides, which coexist in the highly fractured and metasomatized garnet (Figure 4a,b); SchB is granular scheelite within both ZK2002 and ZKB20S samples (Figure 4c,d); while SchC mostly occurring in ZKB20S sample is subhedral to anhedral, associated with calcite and clustered stockwork of quartz grains (Figure 4e–h). Therefore, the SchA and SchB scheelites are distributed in exoskarn deposits, with skarn stage minerals and SchC scheelites identified in endoskarn deposit and associated with calcite filled by the later stage minerals.

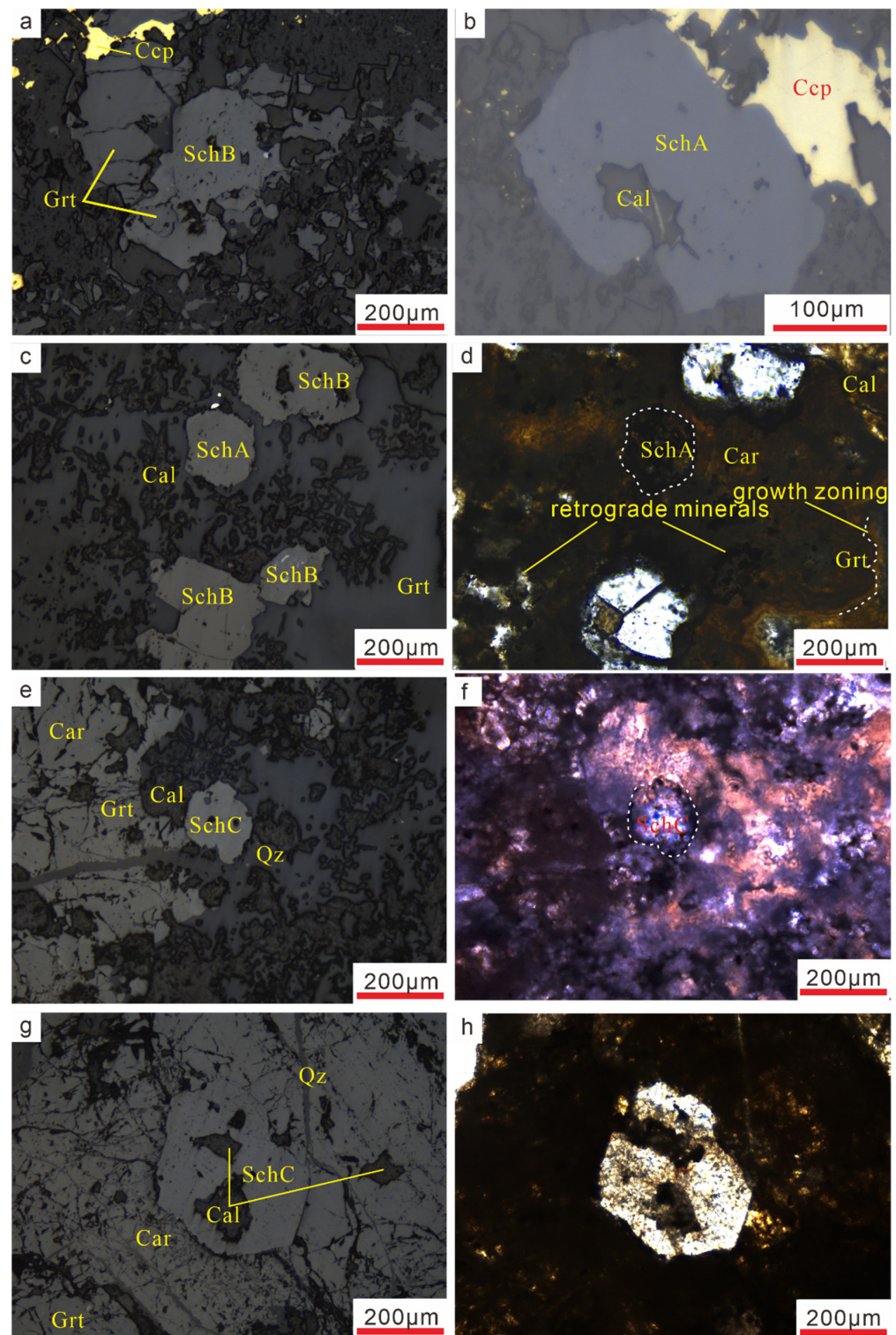


Figure 4. (a,b): Subhedral scheelite grain occurring in ZK2002 (SchA and SchB); (c,d): Subhedral-anhedral scheelites observed in ZK2002 (SchA and SchB), (d) is the crossed polars transmitted light images of image “c”; (e–h): Subhedral to anhedral scheelite occurring in ZKB20S, which are mostly associated with calcite and quartz stockwork (SchC). Abbreviations: Sch—scheelite, Grt—garnet, Ccp—chalcopyrite, Cal—calcite, Car—carbonates, Qz—quartz.

3.2. Analytical Methods

3.2.1. Microprobe Analysis

Major element compositions and elemental mapping were analyzed by electron microprobe analysis (EMPA) at the State Key Laboratory of Geological Processes and Mineral Resources (GPMR), China University of Geosciences (Wuhan), with a JEOL JXA-8100 EMPA equipped with four wavelength-dispersive spectrometers (WDS). An accelerating voltage of 15 kV, beam current of 20 nA and <5 µm-diameter focused beam was used in the analyses.

The raw data were corrected online by using the modified ZAF (atomic number, absorption, fluorescence) correction procedure. Element peaks and backgrounds were measured for all the elements with counting times of 10 s and 5 s, respectively, except for Ti and Mn (peak: 20 s; background: 10 s). The standard samples such as Olivine (Si), Rutile (Ti), Pyrope Garnet (Al, Fe), Rhodonite (Mn), Diopside (Mg, Ca), Jadeite (Na), Sanidine (K), Chromic Oxide (Cr), Nickel (Ni), Celestite (Sr), Barite (Ba, S), Molybdenum (Mo), Copper (Cu), Galena (Pb), and Tungsten (W) were used as reference materials to clarify the consistency of analytical results.

3.2.2. Optical Microscopy Cathodoluminescence (OM-CL)

Polished thin sections of representative samples were examined by OM-CL, using a Leica DM2700P microscope coupled with a CITLMK 5-2 system, at GPMR, China University of Geosciences (Wuhan). The system was operated at 13 kV accelerating voltage and a current density of about 350 µA.

3.2.3. Scanning Electron Microscopy Cathodoluminescence (SEM-CL)

The BSE and CL imaging were performed on polished and carbon-coated samples to characterize the morphology and internal texture of scheelite. The imaging was conducted with a Quanta 450 FEG SEM, equipped with a SDD Inca X-Max 50 and a MonoCL 4+ detector (20 kV accelerating voltage and 20 nA beam current) at GPMR, China University of Geosciences (Wuhan).

3.2.4. LA-ICP-MS Trace Element Analysis

Trace elemental compositions of the Tongshankou scheelite (SchA to SchC) were determined at the National Research Center for Geo-analysis (NRCG), the Chinese Academy of Geological Sciences, Beijing, China by using in situ laser ablation inductively coupled plasma-mass spectrometry (LA-ICP-MS), followed by New Wave NWR-193 laser ablation system coupled to a Thermo Element II mass spectrometer. Prior to entering the ICP, helium (carrying gas) and argon (makeup gas) were combined through a T-connector. Helium (carrier gas) and argon (makeup gas) were mixed via a T-connector prior to the entering of the ICP. The analyzing parameters of LA-ICP-MS demonstrated an accelerating frequency of 10 Hz, beam energy of ~2 mJ and a beam density of 23–25 J/cm² with 35 µm laser spot size. Each analysis comprises a 15 s gas blank measurement (laser-off), followed by a 40 s sample data acquisition (laser-on), and a 15 s cleaning between successive measurements. The ablated materials were flushed in a continuous helium (carrying gas) and argon (makeup gas) combination flow through a T-connector by using an external standard of NIST 612 to correct for linear drift.

4. Results

4.1. Cold Cathodoluminescence Analysis of Scheelite

The inner textural features such as oscillatory zoning and core, mantle and rim texture are difficult to study under a microscope. Therefore, OM-CL analysis has been widely used in research in recent years to examine the inner texture of minerals. However, fine interior texture, such as various phases of mineral formation is difficult to identify. However, scheelite can be analyzed because of its fluorescence characteristics by using cold cathodoluminescence method [5,16]. By using this technique, the detailed texture, filling,

and cutting relationships of several mineral phases are noticed, which can be explained furtherly in discussion part.

4.2. EMPA Mapping of Garnet

Garnets were chosen because of their larger grains and potential association with endoskarn scheelite to explore the major element variation of early-stage skarn minerals. Comparing the proportion of grossular and andradite in garnet, we can apparently demonstrate the redox environment of primary skarn minerals formation [17–19]. The scheelite grains coexisted with garnet and seemed to have a similar growing method from core to rim, so the brighter part of scheelite (Figure 5) can be seen as the faster growing part of scheelite, which was influenced by a high disturbed fluid environment. Therefore, REE analyses are performed to better understand the mineralization of scheelite in Tongshankou deposit.

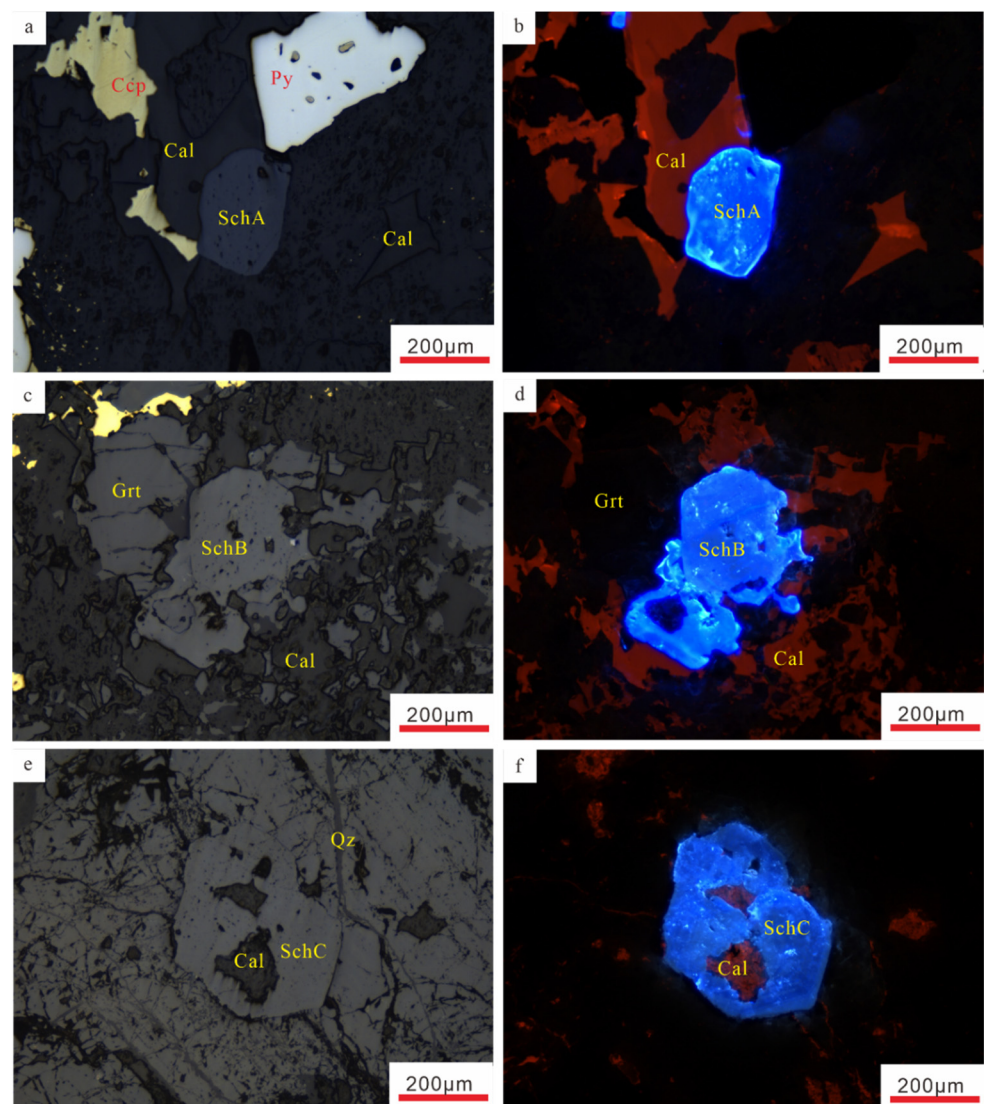


Figure 5. (a,b): SchA is paragenetic with later sulfide minerals, e.g., chalcopyrite; (c,d): SchB occurs with early garnet and sulfides under reflected light microscope in image “c”, and has some lighter part and fractured edge in OM-CL image “d”; (e,f): SchC mainly coexists with garnet and is obviously filled in and traversed by calcite and quartz. Abbreviations: Sch—scheelite, Grt—garnet, Cal—calcite, Qz—quartz, Ccp—chalcopyrite, Py—pyrite. The images on the left are under the microscope with reflected light, and the right images are OM-CL images.

According to the mapping of garnet, it is so clear that garnet has an evolution tendency from grossular to andradite. When the results of garnet EMPA mapping, major elements, garnets crystallography, and dynamic recrystallization are combined, then distal garnet rims have higher Al and Fe contents (Figure 6), which can be seen as regeneration from grossular to andradite. Therefore, these crystallographic processes reveal the hydrothermal evolution that has effects on scheelites.

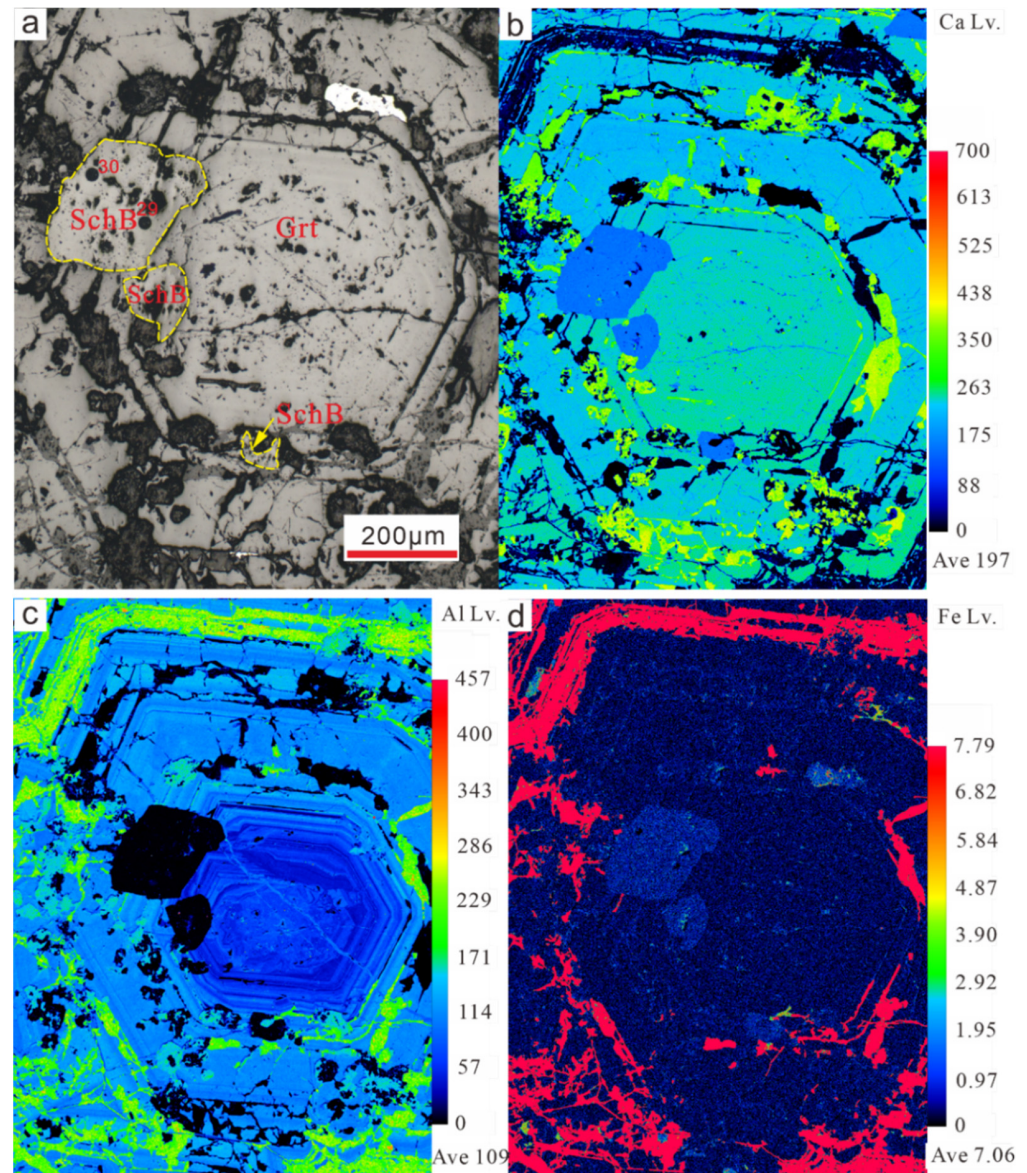


Figure 6. (a): Image taken under the microscope of SchB, which coexists with garnet that could have grown in a similar disturbed environment during garnet formation; (b–d): SchB has an evolution tendency from inner grossular zones (which has relative lower Fe content) to andradite zones within distal rims (which has obvious higher Fe content). This can result from a highly disturbed growing environment, and andradite crystallized faster than grossular in this environment [20].

4.3. Major and Trace Elements in Scheelites

The 62 EMPA results are summarized in Table 1. SchA has the highest WO_3 contents (average of 78.5 wt.%) and SchB has around 75.8 wt.% in average, while the SchC has the lowest WO_3 contents (74.6 wt.% in average), respectively.

Table 1. Results of major element analysis in scheelite from the Tongshankou deposit (wt.%).

Sample No.	Spot No.	WO ₃	MoO ₃	CaO	MnO	SiO ₂	P ₂ O ₅	FeO ^T	Total
ZK2002-1	1	68.60	8.540	20.97	bdl	0.160	0.380	0.070	98.70
	2	56.26	20.11	22.63	bdl	0.160	0.430	0.470	100.1
	3	50.01	24.67	23.40	0.020	0.130	0.530	0.60	99.36
	4	52.03	23.26	22.85	bdl	0.180	0.460	0.190	98.97
	5	69.26	8.120	20.86	0.030	0.180	0.340	0.090	98.88
	6	73.92	5.610	19.37	bdl	0.300	0.340	0.660	100.2
ZK2002-1	1	75.02	3.370	20.56	bdl	0.200	0.230	bdl	99.38
	2	74.75	3.750	20.76	bdl	0.210	0.330	0.020	99.81
	3	74.82	4.010	20.76	0.060	0.180	0.270	0.030	100.1
	4	75.01	3.720	20.67	0.020	0.200	0.240	0.020	99.88
	5	70.44	7.220	20.88	0.020	0.160	0.350	bdl	99.07
	6	74.07	4.320	20.65	bdl	0.200	0.330	0.060	99.63
	7	75.11	3.820	20.94	0.020	0.200	0.300	0.020	100.4
	8	72.07	6.320	21.27	bdl	0.190	0.310	0.100	100.3
ZK2002-2	1	78.20	0.330	20.09	bdl	0.200	0.310	0.050	99.18
	2	79.88	0.300	19.93	bdl	0.230	0.350	0.180	100.9
	3	79.05	0.340	19.97	0.050	0.200	0.260	bdl	99.87
	4	78.26	0.290	19.96	bdl	0.200	0.350	0.010	99.08
	5	78.55	0.220	20.05	0.030	0.200	0.260	0.130	99.43
	6	78.00	1.090	20.17	bdl	0.200	0.280	0.050	99.79
	7	78.13	1.240	20.33	0.010	0.230	0.280	bdl	100.2
	8	79.33	0.270	19.97	0.050	0.240	0.330	0.030	100.2
	9	76.42	1.860	20.14	bdl	0.190	0.240	0.080	98.93
	10	74.49	3.700	20.46	0.030	0.180	0.300	0.030	99.18
	11	78.51	0.520	20.13	0.010	0.200	0.350	0.040	99.76
	12	77.66	0.630	19.97	0.030	0.190	0.340	0.040	98.85
	13	77.38	1.230	20.17	0.010	0.220	0.310	bdl	99.31
	14	78.04	0.510	20.11	bdl	0.210	0.310	0.070	99.25
	15	78.07	0.880	20.18	bdl	0.200	0.310	0.390	100.0
	16	76.94	1.630	20.09	bdl	0.190	0.250	0.090	99.19
	17	76.99	1.620	19.98	0.020	0.220	0.270	0.320	99.42
	18	74.60	4.020	20.45	bdl	0.200	0.360	0.020	99.65
	19	78.92	0.670	20.11	0.030	0.200	0.320	bdl	100.3
	20	78.39	0.870	20.24	bdl	0.160	0.260	0.080	100.0
	21	79.04	0.360	20.05	0.050	0.200	0.280	0.170	100.2
	22	69.85	8.010	21.12	bdl	0.200	0.250	0.030	99.45
	23	75.48	3.000	20.60	bdl	0.250	0.320	bdl	99.66
	24	78.83	0.270	19.60	bdl	0.230	0.270	bdl	99.21
	25	75.75	2.950	20.71	bdl	0.160	0.310	0.020	99.90
	26	78.60	1.130	20.53	0.030	0.220	0.240	0.090	100.8
	27	75.53	3.160	20.29	bdl	0.200	0.320	0.080	99.58
	28	77.42	1.360	20.20	0.060	0.200	0.280	0.100	99.63
	29	76.25	3.070	20.55	bdl	0.200	0.280	0.020	100.4
	30	68.69	9.280	21.25	bdl	0.180	0.380	bdl	99.78
	31	76.40	2.940	20.15	bdl	0.200	0.340	0.030	100.1
	32	75.50	3.160	20.19	bdl	0.200	0.330	bdl	99.37

Table 1. Cont.

Sample No.	Spot No.	WO ₃	MoO ₃	CaO	MnO	SiO ₂	P ₂ O ₅	FeO ^T	Total
B20SZK	1	74.61	3.900	20.14	bdl	0.210	0.260	0.010	99.12
	2	76.47	3.180	20.37	0.020	0.170	0.220	0.080	100.5
	3	78.96	1.190	20.05	0.010	0.210	0.230	bdl	100.6
	4	75.01	2.570	20.24	bdl	0.220	0.280	bdl	98.32
	5	75.40	3.220	20.41	0.010	0.200	0.230	bdl	99.47
	6	76.01	3.130	20.26	bdl	0.180	0.300	0.020	99.89
	7	76.94	0.990	20.27	bdl	0.240	0.210	0.030	98.67
	8	75.03	2.720	20.18	0.010	0.200	0.280	bdl	98.42
	9	66.19	11.03	21.65	bdl	0.150	0.370	0.040	99.43
	10	73.65	4.420	20.87	bdl	0.170	0.290	bdl	99.39
	11	75.35	3.110	20.55	bdl	0.200	0.270	bdl	99.48
	14	77.72	1.260	20.43	bdl	0.230	0.290	0.070	100.0
	15	75.71	2.690	20.49	bdl	0.200	0.210	0.020	99.31
	16	75.69	2.600	20.33	bdl	0.190	0.280	0.010	99.11
	17	64.96	11.63	21.48	0.030	0.160	0.380	bdl	98.64
	18	76.28	2.670	20.26	0.020	0.180	0.250	bdl	99.65

bdl = below detection limit. Detection limit of EMPA is 0.01 wt.%. FeO^T: total contents of Fe.

Molybdenum is more susceptible to redox conditions than W element due to its two distinct electric valences. SchB has the highest average MoO₃ concentration (4.85 wt.%), as well as the highest single grain content (approximately 25 wt.%), while MoO₃ contents of SchC are often greater than those of SchA (Figure 7 and Table 1).

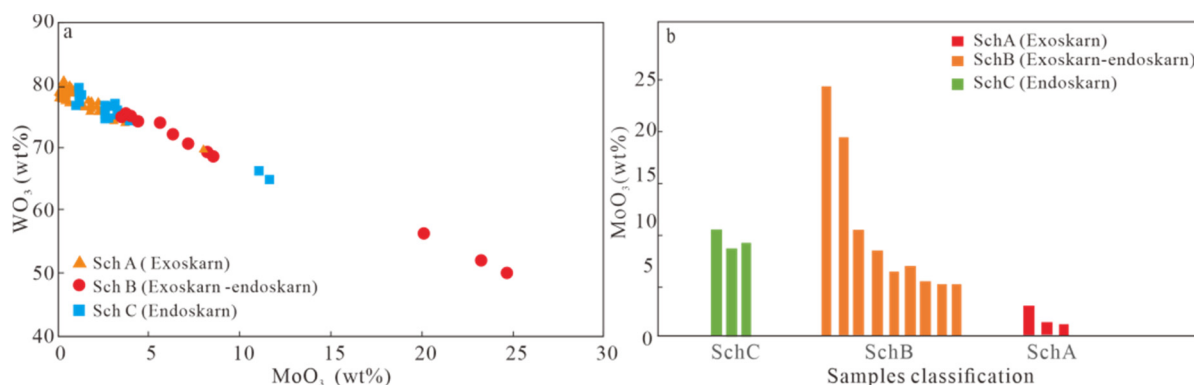


Figure 7. WO₃ vs. MoO₃ contents in SchA–SchC at Tongshankou deposit, showing the relationship between major elements (WO₃ and MoO₃) of scheelite. (a) Diagram of MoO₃ vs. WO₃ in scheelites from the Tongshankou deposit, showing the negative correlation between WO₃ and MoO₃ (b) Histogram of MoO₃ content for SchA, SchB and SchC, showing the various MoO₃ contents.

SchA, mainly within exoskarn, has the highest WO₃ contents and lowest MoO₃ contents, indicating a reducing crystallization state (Figure 7a). The MoO₃ concentration and occurrence of 15 scheelite grains were categorized based on their substantial differences (Figure 7b). Furthermore, under a microscope and in OM-CL images, these distinct grains exhibit obvious mineralogical features that may be identified. The MoO₃ concentrations in SchC (inside the garnet skarn) are higher compared with SchA and SchB formed within the sulfides stage and were mostly observed in the molybdenum ore sample, so it has the highest MoO₃ content.

Strontium, Pb, Nb, Na and Ba are the trace elements observed in scheelite with considerable abundances. There are many spots where Na concentrations are below the detection limit, while within the same skarn Nb and Sr have relatively similar concentrations. In Tongshankou deposit, Sr contents of scheelites range variously and have an average of 340.4 ppm. Niobium abundances are about 13 ppm (average) within exoskarn, whereas

they are about 28 ppm (average) in endoskarn (Table 2). Σ REE substitution mechanism analyses can be applied for the correlation of Nb and Sr elements abundance.

Table 2. Results of trace element analysis in scheelite from Tongshankou deposit (ppm).

Sample No.	Spot No.	Na	Nb	Sr	Ba	Pb
ZK2002-1	1	13.99	1.800	369.7	0.312	5.250
	2	bdl	1.309	357.8	0.324	2.660
	3	bdl	6.788	482.2	0.168	1.364
	4	bdl	7.078	482.6	0.105	1.299
	5	48.80	5.720	465.9	0.160	1.097
	6	4.180	6.681	462.3	0.066	1.389
	7	bdl	4.268	433.6	0.124	1.200
	8	50.75	9.946	611.3	0.165	0.974
	9	19.45	12.61	632.2	0.243	0.802
	10	27.64	11.01	589.1	0.424	1.001
	11	6.360	9.784	631.2	0.224	0.850
	12	bdl	2.393	446.8	0.255	1.036
	13	17.24	3.718	402.0	0.175	1.210
	average	23.55	6.390	489.8	0.210	1.550
ZK2002-2	1	bdl	55.24	144.9	0.13	4.905
	2	4.770	37.11	165.7	0.037	7.006
	3	16.46	15.71	175.1	0.002	5.432
	4	12.84	56.28	130.0	0.026	3.722
	5	bdl	12.68	185.1	0.155	3.888
	6	bdl	25.69	176.9	0.048	2.390
	7	25.00	29.44	156.9	0.096	1.897
	8	30.47	38.84	117.7	bdl	3.088
	9	bdl	24.34	242.4	0.116	2.880
	10	bdl	9.799	277.7	0.264	3.522
	11	bdl	25.27	140.0	0.101	2.040
	12	17.74	13.19	306.9	0.061	3.963
	13	14.02	4.300	310.1	0.067	3.969
	14	bdl	3.250	290.4	0.209	4.071
	15	bdl	13.80	447.5	0.240	3.951
	16	28.66	9.447	496.6	0.135	4.138
	17	31.79	4.265	454.6	0.111	5.155
	18	130.65	10.74	334.7	0.122	2.761
	19	bdl	17.35	241.8	0.249	3.902
	20	bdl	3.139	183.9	0.290	5.836
	21	50.55	3.717	216.4	0.191	3.506
	22	132.66	4.092	289.5	0.004	4.477
	23	130.21	7.683	320.9	0.034	4.193
	24	bdl	14.13	287.9	bdl	2.98
	25	bdl	1.235	235.2	bdl	3.915
	26	bdl	1.485	210.5	0.029	3.548
	27	20.98	15.54	167.1	0.030	2.133
	28	6.990	26.57	439.6	0.061	3.327
	29	39.18	15.01	294.7	0.143	9.046
	30	1.540	19.05	199.8	0.089	1.635
	31	bdl	1.340	217.0	0.039	3.472
	32	76.79	1.912	196.3	0.197	3.343
	average	42.85	16.30	251.7	0.110	3.880

Table 2. Cont.

Sample No.	Spot No.	Na	Nb	Sr	Ba	Pb
ZKB20S	1	bdl	8.770	495.8	bdl	1.163
	2	bdl	13.33	526.3	0.183	1.175
	3	24.85	7.682	538.4	0.086	1.336
	4	6.270	11.87	545.5	bdl	1.185
	5	106.8	26.56	542.4	0.295	1.402
	6	bdl	1.566	336.8	0.099	1.617
	7	44.52	1.236	376.4	0.228	1.941
	8	46.06	12.07	334.6	0.397	2.633
	9	54.15	28.95	303.4	0.329	2.420
	10	bdl	41.50	378.1	0.158	1.985
	11	36.06	89.56	263.0	0.229	2.570
	12	bdl	48.12	278.5	0.084	2.459
	13	19.05	41.06	283.6	0.220	3.160
	14	29.49	45.39	284.8	0.124	3.570
	15	8.940	52.53	384.1	0.073	2.468
	16	22.80	12.93	535.4	0.123	1.978
	17	28.12	35.90	286.1	0.184	2.353
	average	35.60	28.18	393.7	0.187	2.083

bdl = below detection limit.

4.4. Rare Earth Element Geochemistry

REE geochemistry is an important factor that helps to examine detailed geochemistry processes [21–27]. La/Yb ratio is considered to indicate LREE and HREE fractionation, whereas La, Ce and Eu anomalies represent magmatic or hydrothermal fluid redox conditions [28–33]. The Tongshankou deposit also has a porphyry system that is related to oxidized magma [2,3,6,12,34]. The diorite and skarn are both enriched in LREE and depleted in HREE with a relatively strong slope of LREE type and a weak negative Eu anomaly [34,35]. To better examine the scheelites REE geochemistry, the Eu anomaly was focused to understand the evolutionary process (Figure 8).

Several points have some elements below the detection limit, which made Lu seem to have abnormal positive anomalies. Consequently, the “bdl” points have been wiped out to weaken the test errors.

Compared with REE characteristics of scheelites from other skarn deposits [36–41], analyzed results of samples in the Tongshankou deposit are mostly Eu positive. SchA and B have higher Σ REE and stronger Eu positive anomalies and SchC usually has similar LREE-enriched and HREE-depleted REE patterns.

Scheelites in the Tongshankou skarn deposit have the evolution process from “flat” and relatively high Σ REE contents to enrichment in LREE and depletion in HREE patterns, which is consistent with bulk rock background value.

In addition, the trace element fluctuation process has been examined to better understand the substitution mechanism during scheelite crystallization. Generally, there are three different substitution mechanisms: $2\text{Ca}^{2+} \rightleftharpoons \text{REE}^{3+} + \text{Na}^+$ (1); $\text{Ca}^{2+} + \text{W}^{6+} \rightleftharpoons \text{REE}^{3+} + \text{Nb}^{5+}$ (2); $3\text{Ca}^{2+} \rightleftharpoons 2\text{REE}^{3+} + \square\text{Ca}$ ($\square\text{Ca}$ = Ca site vacancy) (3) [36,42,43] involved in scheelite crystallization. Nb vs. REE-Eu + Y and Eu vs. Eu/Eu* ratios have been plotted to demonstrate the substitution mechanism of scheelite in the Tongshankou deposit (Figure 9c). Plots of Nb vs. Σ REE-Eu + Y (Figure 9a), Σ REE-Eu + Y are used to eliminate Eu anomaly influence. Eu_N vs. $\text{Eu}_N^*/\text{Eu}^*$ were used to preclude Ca content influence in the mechanism (3) (Figure 9b,c) [44], because Eu^{2+} ions tend to enter the scheelite lattice to fill in the Ca vacancy.

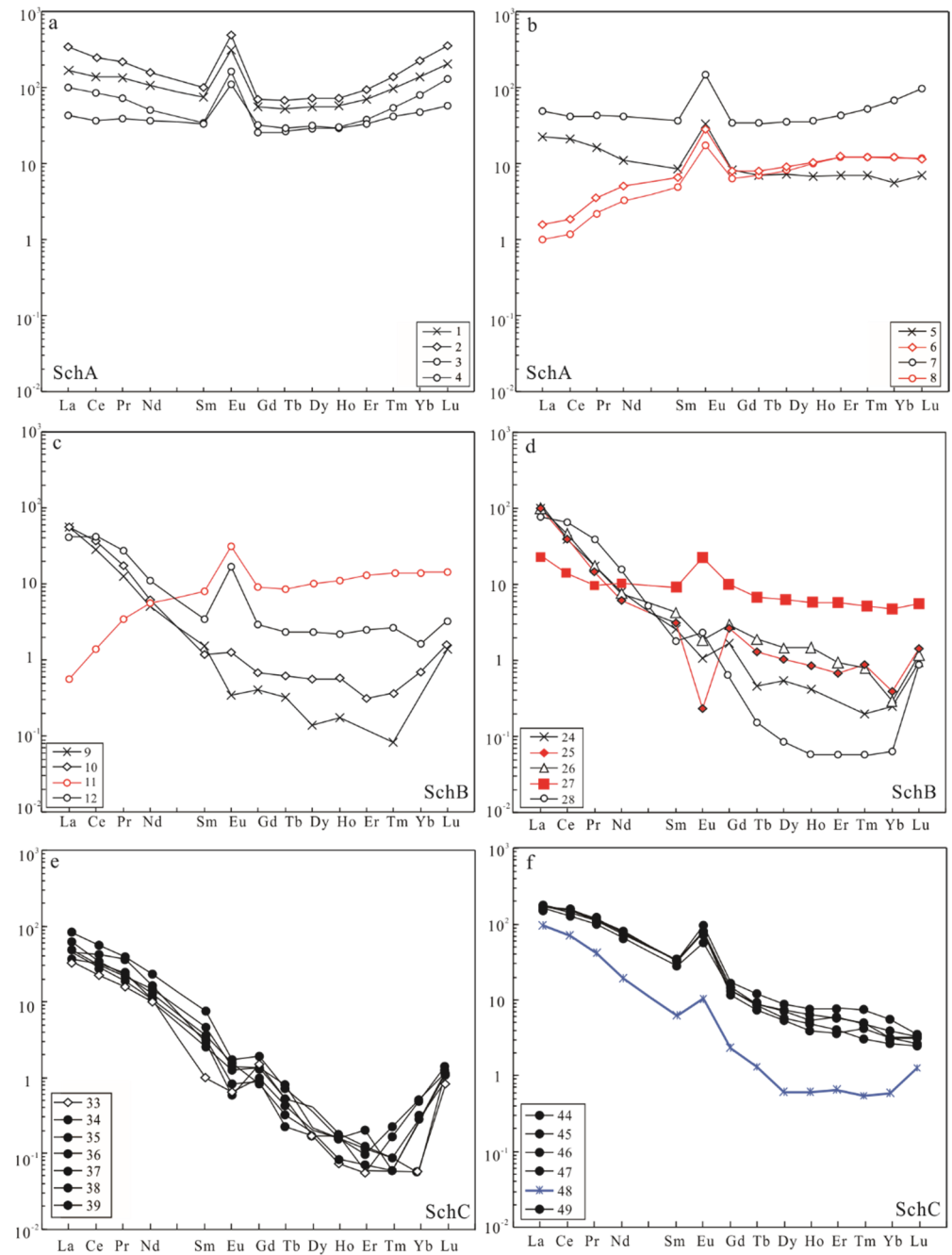


Figure 8. (a,b): SchA-higher Σ REE and more predominant positive Eu anomalies; (c,d): SchB-obvious different points, and red curves are associated with brighter mantle and rim in SEM-CL images, and these parts in SEM-CL or OM-CL have different optical properties; (e,f): SchC-within endoskarn, which mostly have LREE-enriched and HREE-depleted pattern such as bulk rock in porphyry intrusions, and some positive Eu anomalies would probably be caused by fluid. The normalization values were taken from Taylor and McLennan (1985) [33].

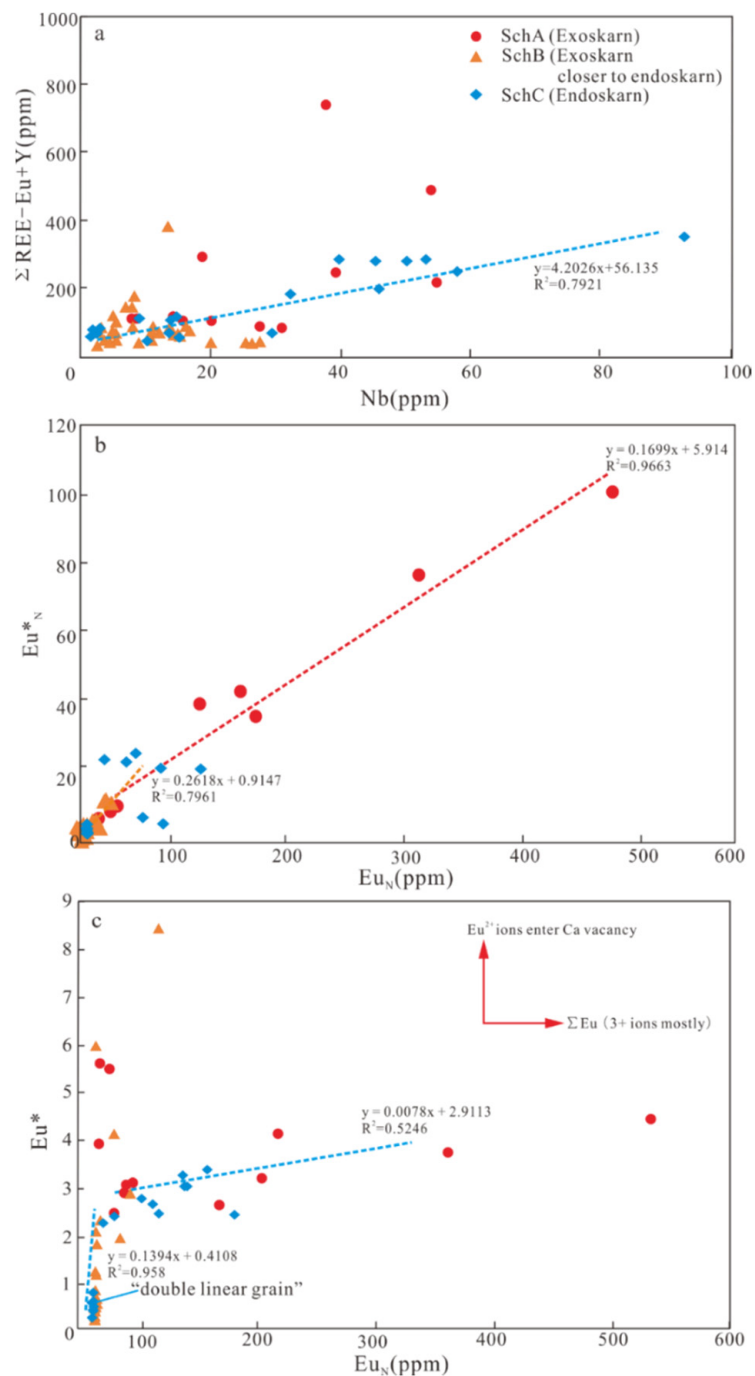


Figure 9. Trace element plots of Nb and REE characteristics showing the substitution mechanism (The normalization values were taken from Taylor and McLennan (1985) [33]). (a) Diagram of Nb vs. $\Sigma \text{REE-Eu} + \text{Y}$, showing the substitution mechanism in scheelite. (b) Diagram of Eu_N vs. Eu^*_N , showing the correlation between Eu^* and Eu^*_N . (c) Diagram of Eu_N vs. Eu^* , indicating the Eu^*_N is composed of Eu^{2+} and Eu^{3+} .

In the substitution mechanism (2), SchC exhibits a clear linear trend, indicating that it is the main mechanism in endoskarn mineralization (Figure 9a). The majority of SchA and a portion of SchB exhibit a correlation between Eu_N and Eu/Eu^* , implying that Eu anomalies in SchA and SchB should be triggered by $3\text{Ca}^{2+} \rightleftharpoons 2\text{REE}^{3+} + \square\text{Ca}$ ($\square\text{Ca}$ = Ca site vacancy) (Figure 9b). The fact that Eu anomaly has increased together with ΣREE , indicates that Eu has a more distinct entry mechanism than other REEs (Eu^{2+} ions enter the Ca vacancy). During crystallization, some SchC grains, particularly the “double linear

grain” may have numerous substitution mechanisms (Figure 9c). SchA has a clear linear pattern, and the data was plotted to find if it was corresponding to mechanism (3), and it has a strong correlation with a coefficient of 0.96.

5. Discussion

5.1. W-Mo Substitution Mechanism

The substitution of W-Mo contents in scheelite has been studied in detail, which is one of the most important influencing factors for the formation of tungsten ore [45,46] (Figure 7a). Scheelites have been shown to exhibit various mineralization processes even within the same sample [5,47]. Although W and Mo show a clear negative correlation (W^{6+} and Mo^{6+} replacement) (Figure 7a), redox influences in the concentration of W and Mo are not clearly demonstrated. In general, oxidized scheelite with more Mo content coexists with skarn minerals that formed earlier than minerals in oxidation stage, and reducing scheelite coexists with sulfides, quartz and calcite. Scheelite within endoskarn contains higher Mo contents and lower W contents, which may indicate an early oxidized fluid. When the distal skarn is concerned, reducing scheelite with a higher W content and a lower Mo content is crystallized with sulfides and ore-bearing quartz veins (Figure 7b).

The substitution mechanisms (3) of $Ca^{2+} + W^{6+} \rightleftharpoons REE^{3+} + Nb^{5+}$ (2) and $3Ca^{2+} \rightleftharpoons 2REE^{3+} + \square Ca$ ($\square Ca$ = Ca site vacancy) were compared (Figure 9c), and element plots were used to determine the major mechanism during ore formation. The results show that mechanism (2) controls the progression of SchC, which is mostly based on linear and fine correlation, while mechanism (3) controls the formation of SchA and SchB. Scheelites may have undergone numerous substitutions during the ore formation as a result of the changing redox conditions of environment fluid. Actually, substitution mechanisms (2) and (3) have shown to be active (or present) in a single grain of SchC scheelite type. Further investigation of its texture under SEM-CL images and OM-CL images revealed that it originally had distinct later filling and cutting texture with different optical properties (another generation of scheelite) and its mottled oscillatory zoning should be evidence of this process.

5.2. Multistage Ore-Forming Process—“Double Linear Grain”

“Double linear grain” refers to the progression of two of three substitution mechanisms in one grain, which is most common in endoskarn. The grain is assumed to have undergone multi-stage mineralization (SchI-early stage and SchII-late stage) by analyzing its internal texture in cold cathodoluminescence (Figure 10). It is clear that two substitution mechanisms played an important role in this “double linear grain” (Figure 9c).

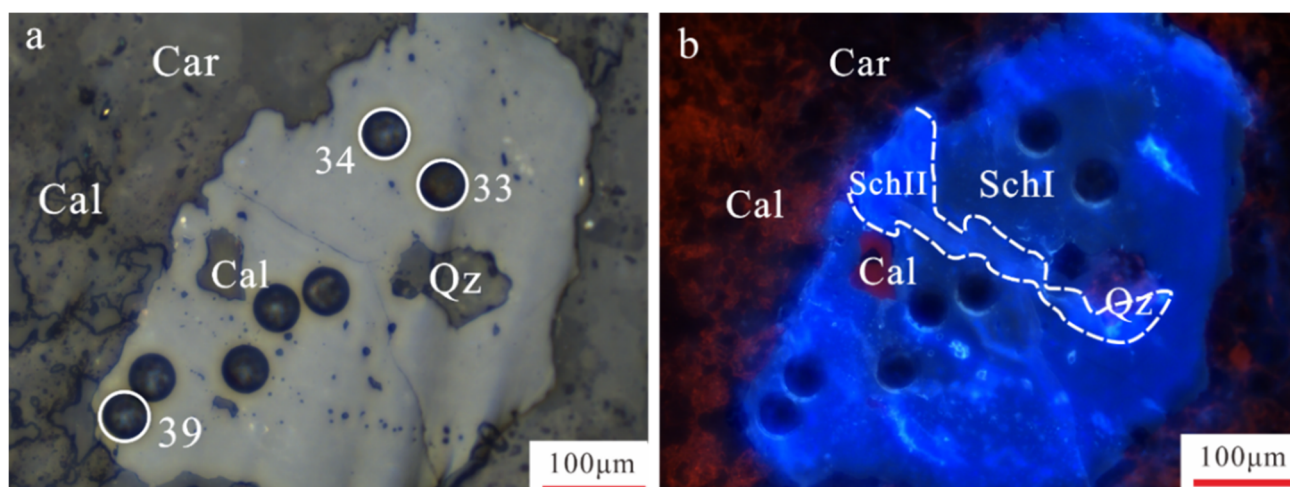


Figure 10. Characteristics of the typical “double linear grain” in SchC within endoskarn, showing the filling texture of late scheelite II into early scheelite I. (a) The image of the double linear grain taken under the microscope by reflected light (b) The OM-CL image of the double linear grain.

These kind of grains can be evidence of at least two substitutions occurring during the formation of a single scheelite. In fact, the other two of the three selected SchC grains have a lower slope linear trend such as SchA (Figure 9c), indicating disseminated, cutting texture and oscillatory zoning. These textures may represent different stages of scheelite mineralization and their own crystallization process.

Eu_N vs. Eu/Eu^* plots are used in combination with REE partition mapping to determine if the entry of Eu^{2+} ions was the primary factor for Eu/Eu^* formation (Figures 8a–d and 9a–c). Higher linear relationship indicates that Eu ions have more than “ Eu^{3+} ” form when entering scheelite lattice compared to other REE (as shown in mechanism (3)) (Figure 9b). At a late stage, scheelites have similar substitution and forming mechanism, which can be seen as a transition from endoskarn to exoskarn.

The slope of linear trend in plots would be lower (at the lowest it would be a horizontal line) if the Eu_N was mostly made up of the Eu^{3+} ions. However, it was significantly greater in Figure 9b, indicating that Eu^{2+} ions penetrate the lattice mostly in exoskarn SchB and SchA, rather than endoskarn SchC (relatively oxidating).

In fact, this could have originated from the geochemical characteristic of the Tongshankou porphyry source region: High Sr/Yb ratio at the average of 73.5, enrichment in LREE, depletion in HREE, high silica-alkali ratios [34,48,49], which illustrates the typical adakite signal in Tongshankou intrusions. The Sr/Yb ratio can be considered as an overview of the P-T conditions source region [50], and the high Sr/Yb and weak negative Eu anomaly revealed very little fractional crystallization of plagioclase in the source region of Tongshankou magma [36,51,52]. Therefore, the relatively weak Eu anomaly in SchC (lower values compared with SchA and SchB) could be linked to the geochemical characteristics of intrusions. Eu ions were mostly induced to enter plagioclase during early skarn mineralization. When early formed plagioclase dissolved and was released into the fluid, then Eu re-entered the hydrothermal fluid with other metallogenic elements and was transported to the exoskarn. In the exoskarn, relative reducing conditions caused Eu^{2+} to be more abundant than Eu^{3+} , and mechanism (3) is dominated by crystallization. Therefore, the positive Eu anomalies are widely distributed in REE patterns of Sch A and B (Figure 8a–d).

However, the uncoordinated spots continued to appear in the REE distribution pattern, and these spots were more prominent in those grains with distinct core, middle and rim partition and had strong positive Eu anomalies (Figure 8c,d).

5.3. Internal Texture of “Uncoordinated” Grains

These uncoordinated spots points are mostly observed in OM-CL images as zones with lighter optical properties as compared to others, but there is no obvious cutting and filling texture under a microscope (Figure 11). It revealed that a random distribution of crystal-growing environment (hydrothermal fluid) eventually led to the formation of composite scheelite grains. Therefore, these uncoordinated spots can be seen as a special footprint indicating multi-stage hydrothermal mineralization of skarn deposit. In relation to previous discussion of substitution mechanisms, the Eu anomaly should be an indication of late-stage reducing hydrothermal fluid activity [44,46].

The tungsten concentration of reduced scheelite bearing skarns is greater than that of oxidized scheelite bearing skarns. [16,46,48]. The reducing hydrothermal fluid formed different types of scheelite grains in the early skarn stage mineralization within the endoskarn. The reducing W skarn deposit has significantly more tungsten concentration because of the fluid transportation process. Tungsten should be carried better in this process than under oxidized conditions because tungsten can be carried in ionic complex form during transportation, and competes with Mo, which has the same 6+ electronic valence. This may elucidate why scheelite is commonly associated with sulfides and reduced minerals, particularly molybdenite. The mafic enclaves in the Tongshankou district have the highest concentration of W [8]. Such mafic enclaves hosted in the ore-forming porphyries were

most likely generated by a magma mixing process [6]. Therefore, W has a different magma source from the oxidized porphyry magma.

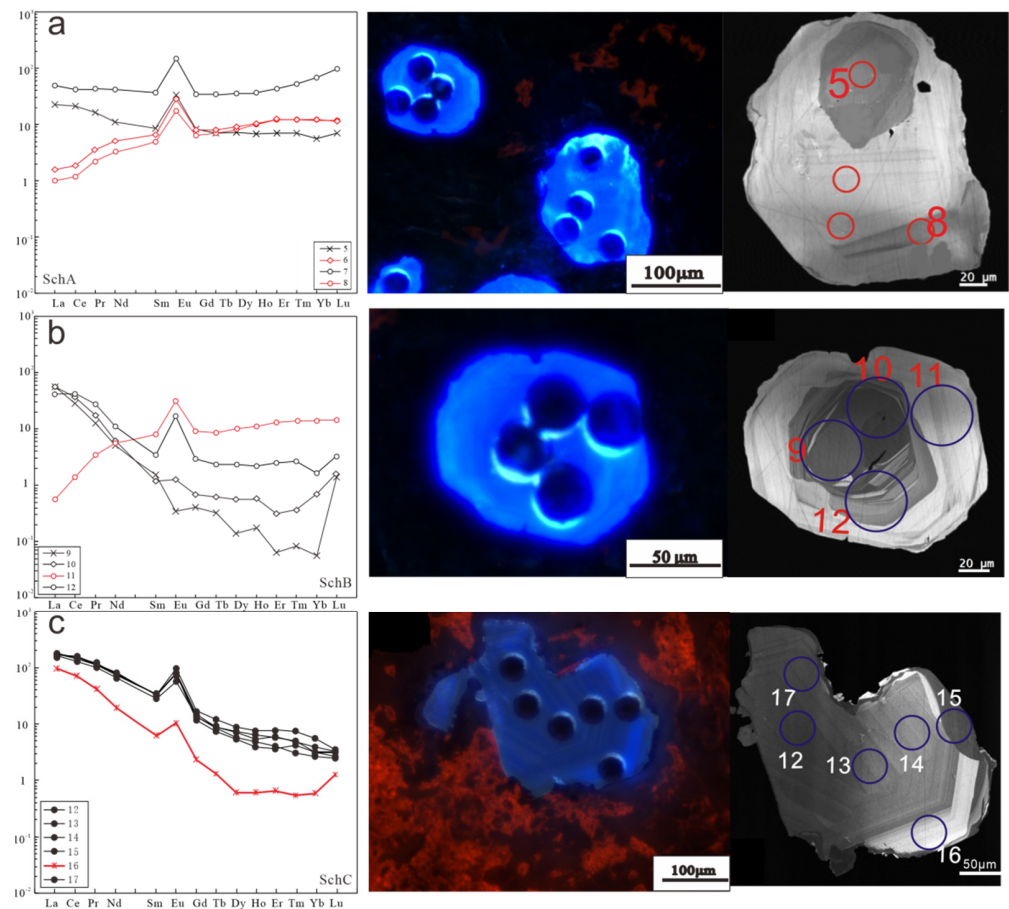


Figure 11. The characteristics of red curves, which are “uncoordinated” among SchA (a), SchB (b), SchC (c): diagrams on the left are REE distribution patterns of scheelite, the middle photos are cold cathodoluminescence images and the photos on the right are corresponding SEM-CL images of the grains. The normalization values were taken from Taylor and McLennan (1985) [33].

6. Conclusions

This research presents the first detailed investigation of scheelites in skarns at the Tongshankou deposit where three types of scheelites (SchA, B and C) have been identified. The following geochemical and CL features of different scheelites can be concluded:

1. The geochemistry and OM-CL show that the W mineralization has been highly disrupted during the formation of scheelite. The skarn mineralization system has an apparent evolution in the redox environment from endoskarn (SchC) to the distal exoskarn (SchA). W-Mo concentrations have fluctuation due to the crystallization of multi-stage minerals. SchC is considered to have similar Σ REE features as intrusions with the negative Eu anomaly, whereas SchA and SchB have higher Σ REE characteristics and a comparatively high positive Eu anomaly.
2. “Double linear grain”, postulated for the first time in this work, could be one of the evidences of two substitution mechanisms in a single scheelite grain, which is the typical characteristic of SchC. In addition, the cutting and filling texture in scheelites are also prominent in OM-CL images. Early endoskarn scheelites were dominated by mechanism $\text{Ca}^{2+} + \text{W}^{6+} \rightleftharpoons \text{REE}^{3+} + \text{Nb}^{5+}$ (2), in scheelite crystallization and there was no appropriate reducing environment to sustain mechanism (3) $3\text{Ca}^{2+} \rightleftharpoons 2\text{REE}^{3+} + \square\text{Ca}$ ($\square\text{Ca}$ = Ca site vacancy). The reducing fluid metasomatized the carbonate

- strata, traversed and regenerated some earlier scheelites following mechanism (3), and caused a positive Eu anomaly in the late skarn stage.
3. The ore formation at the Tongshankou area is a multistage process, including a porphyry system at ~143 Ma and a skarn system at ~140 Ma. The porphyry system has an obvious priority relationship in time scale compared with the skarn system and it was probably the source of both the metallogenic element and the hydrothermal fluid. According to this study, the oxidation mineralization of Cu and Mo may have different magma sources for W. Scheelites formed with mechanism (2) during the early skarn stage mineralization within endoskarn, when there was no appropriate reducing environment for fluid transportation. Both the mechanism $\text{Ca}^{2+} + \text{W}^{6+} \rightleftharpoons \text{REE}^{3+} + \text{Nb}^{5+}$ (2) and mechanism $3\text{Ca}^{2+} \rightleftharpoons 2\text{REE}^{3+} + \square\text{Ca}$ ($\square\text{Ca}$ = Ca site vacancy) (3), indicate fluctuation in ΣREE in Tongshankou scheelite, suggesting multi-stage mineralization: At the first stage, mechanism (2) hosted within endoskarn proceeded through mechanism (3), and the ΣREE increased throughout the single systematical skarn mineralization. Those grains with uncoordinated REE characteristics might be indicative of a reducing metallogenic fluid entering the skarn system during the late stage of evolution.
 4. The association of skarn W mineralization with an oxidized porphyry Cu (Mo) deposit in Tongshankou could be explained by magma sources coming from various locations and being transported with distinct redox fluids. Endoskarn and exoskarn scheelites exhibit distinct growing environments and W-Mo concentrations, indicating that W may have a favorable transportation mechanism from an oxidation to a reducing environment. Mo-rich scheelites are formed from an early metallogenic fluid and when it evolved at a later stage, magma from different source regions upwelled, generating a more reducing environment, though contamination by some earlier-formed intrusions.

Author Contributions: Conceptualization, R.-Z.Z. and M.-F.W.; methodology, R.-Z.Z. and J.-P.W.; software, R.-Z.Z. and X.-Y.S.; validation, M.-F.W., H.L.; formal analysis, R.-Z.Z. and X.-Y.S.; investigation, R.-Z.Z., M.-F.W. and X.-Y.S.; resources, M.-F.W. and H.L.; data curation, M.-F.W., H.L. and Z.U.; writing—original draft preparation, R.-Z.Z. and X.-Y.S.; writing—review and editing, R.-Z.Z., M.-F.W., H.L. and Z.U.; visualization, M.-F.W., J.-P.W., and H.L.; supervision, M.-F.W., H.L. and Z.U.; funding acquisition, M.-F.W. All authors have read and agreed to the published version of the manuscript.

Funding: This research was funded by the National Natural Science Foundation of China, grant number 41272097, the Central Universities, China University of Geosciences (Wuhan), grant number CUGCJ1711, National Key Research and Development Program of China, grant number 2016YFC0600508, National Science and Technology Major Project of the Ministry of Science and Technology of China, grant number 2017ZX05009-002, and Hainan key Laboratory of Marine Geological Resources and Environment, grant number HNHYZZYYHJKF004.

Data Availability Statement: All data generated or analyzed during this study are included in this published article.

Acknowledgments: The authors thank Lu Wang for helping with the SEM-CL imaging, Wei Wang and Xiao-nan Guo for their field assistance, and Di Zhang and Sheng-ren Chang for their help for analysis. Also, Cenozoic Geoscience Editing & Consultancy (Australia) is acknowledged for its language editing service. We are grateful to anonymous reviewers and the Editor in Chief for their valuable comments and suggestions that improve the quality of this paper.

Conflicts of Interest: The authors declare no conflict of interest.

References

1. Yang, Z.M.; Hou, Z.Q.; Zhou, L.M.; Zhou, Y.W. Critical elements in porphyry copper deposits of China. *Chin. Sci. Bull.* **2020**, *65*, 3653–3664. (In Chinese with English abstract) [[CrossRef](#)]
2. Zhu, Q.Q.; Xie, G.Q.; Han, Y.X. Characteristics of Tungsten Mineralization from the Tongshankou Skarn-Porphyry Cu (Mo) Deposit in Daye, Hubei Province, and Its Geological implications. *Earth Sci.* **2019**, *44*, 441–455. (In Chinese with English abstract)

3. He, D.; Tan, J.; Liu, X.Y.; Zhang, M.; Zhao, B.; Chen, Y.; Zhao, Y.Y. Significance of inclusions and fluid evolution of the porphyry-skarn copper-molybdenum deposit in Tongshankou, Daye, Hubei. *Bull. Geol. Sci. Technol.* **2020**, *39*, 97–108. (In Chinese with English abstract)
4. Duan, D.F. Geological Character and Ore Genesis of Cu-Polymetallic Deposits Surrounding Yangxin Batholith. Ph.D. Thesis, China University of Geosciences (Wuhan), Wuhan, China, 2019. (In Chinese with English abstract)
5. Han, J.S.; Chen, H.Y.; Hong, W.; Hollings, P.; Chu, G.B.; Zhang, L.; Sun, S. Texture and geochemistry of multi-stage hydrothermal scheelite in the Tongshankou porphyry-skarn Cu-Mo(-W) deposit, eastern China: Implications for ore-forming process and fluid metasomatism. *Am. Mineral.* **2020**, *105*, 945–954. [[CrossRef](#)]
6. Chu, G.B.; Chen, H.Y.; Falloon, T.J.; Han, J.S.; Zhang, S.T.; Cheng, J.M.; Zhang, X.B. Early Cretaceous mantle upwelling and melting of juvenile lower crust in the Middle-Lower Yangtze River Metallogenic Belt: Example from Tongshankou Cu-(Mo W) ore deposit. *Gondwana Res.* **2020**, *83*, 183–200. [[CrossRef](#)]
7. Zhou, T.F.; Fan, Y.; Yuan, F. Advances on petrogenesis and metallogeny study of the mineralization belt of the Middle and Lower Reaches of the Yangtze River area. *Acta Petrol. Sin.* **2008**, *24*, 1665–1678. (In Chinese with English abstract)
8. Zhou, T.F.; Fan, Y.; Wang, S.W.; Noel, C.W. Metallogenic regularity and metallogenic model of the Middle-Lower Yangtze River Valley Metallogenic Belt. *Acta Petrol. Sin.* **2017**, *33*, 3353–3372. (In Chinese with English abstract)
9. Wang, M.F.; Zhao, R.Z.; Shang, X.Y.; Wei, K.T.; An, W.W. Factors controlling Pt-Pd enrichments in intracontinental extensional environment: Implications from Tongshankou deposit in the Middle-Lower Yangtze River Metallogenic Belt, Eastern China. *Ore Geol. Rev.* **2020**, *124*, 103621. [[CrossRef](#)]
10. Chang, Y.F.; Li, J.H.; Song, C.Z. The regional tectonic framework and some new understandings of the Middle-Lower Yangtze River Valley Metallogenic Belt. *Acta Petrol. Sin.* **2019**, *35*, 3579–3591. (In Chinese with English abstract)
11. Zhao, X.F.; Li, J.W.; Ma, C.Q. ⁴⁰Ar-³⁹Ar geochronology of Tongshankou Cu (Mo) deposit in the Southeastern Hubei Fe-Cu Province: Implications for regional metallogeny. *Acta Geol. Sin.* **2006**, *80*, 849–862. (In Chinese with English abstract)
12. Zhai, Y.S.; Yao, S.Z.; Lin, X.D.; Jin, F.Q.; Zhou, X.R. Metallogenic regularity of iron and copper in the middle and lower reaches of the Yangtze River. *Miner. Depos.* **1992**, *11*, 1–12. (In Chinese with English abstract)
13. Shu, Q.A.; Chen, P.L.; Cheng, J.R. *The Geology of Iron and Copper Deposits in Eastern Hubei Province*; Ministry of Metallurgical Industry Publishing House: Beijing, China, 1992; pp. 1–532. (In Chinese with English abstract)
14. Lv, X.B.; Yao, S.Z.; Lin, X.D. The geological characteristics and ore-forming mechanism of Tongshankou skarn- porphyry composite type of copper (molybdenum) ore deposit, Hubei. *Earth Sci.* **1992**, *17*, 171–180. (In Chinese with English abstract)
15. Chu, G.B.; Zhang, S.T.; Zhang, X.B.; Han, J.S.; Zhang, Y.; Cheng, J.M.; Feng, Y.Z. Chlorite chemistry of Tongshankou porphyry-related Cu-Mo-W skarn deposit, Eastern China: Implications for hydrothermal fluid evolution and exploration vectoring to concealed orebodies. *Ore Geol. Rev.* **2020**, *122*, 103531. [[CrossRef](#)]
16. He, J.Y. Mineralogical Characteristics of Ruanjiawan Scheelite Deposit. Master's Thesis, China University of Geosciences (Beijing), Beijing, China, 2020. (In Chinese with English abstract).
17. Zhao, W.W.; Zhou, M.F.; Williams, J.A.; Zhao, Z. Constraints on the uptake of REE by scheelite in the Baoshan tungsten skarn deposit, South China. *Chem. Geol.* **2018**, *477*, 123–136. [[CrossRef](#)]
18. Jiang, X.J.; Chen, X.; Zheng, Y.Y.; Gao, S.B.; Zhang, Z.L.; Zhang, Y.C.; Zhang, S.Z. Decoding the oxygen fugacity of ore-forming fluids from garnet chemistry, the Longgen skarn Pb-Zn deposit, Tibet. *Ore Geol. Rev.* **2020**, *126*, 103770. [[CrossRef](#)]
19. Yin, J.W.; Li, X.J. Characteristics of garnet in Shizhuyuan skarn deposit, Hunan province. *Earth Sci.* **2000**, *25*, 163–171. (In Chinese with English abstract)
20. Gaspar, M.; Knaack, C.; Meinert, L.D.; Moretti, R. REE in skarn systems: A LA-ICP-MS study of garnets from the Crown Jewel gold deposit. *Geochim. Cosmochim. Acta* **2008**, *72*, 185–205. [[CrossRef](#)]
21. Correa, R.S.; Oliveira, C.G.; Dantas, E.L.; Della Giustina, M.E.S.; Hollanda, M. The root zones of the Seridó W-skarn system, northeastern Brazil: Constraints on the metallogenesis of a large Ediacaran tungsten Province. *Ore Geol. Rev.* **2021**, *128*, 103884. [[CrossRef](#)]
22. Fitros, M.; Tombros, S.F.; Kiliyas, S.P.; Kokkalas, S.; Perraki, M.; Skliros, V.; Simos, X.C.; Papaspyropoulos, K.; Avgouropoulos, G.; Williams-Jones, A.E.; et al. REE-enriched skarns in collisional settings: The example of Xanthi's Fe-skarn, Rhodope Metallogenetic Massif, Northern Greece. *Lithos* **2020**, *370*, 105638. [[CrossRef](#)]
23. Yıldırım, E.; Yıldırım, N.; Dönmez, C.; Koh, S.M.; Gunay, K. Mineralogy, Rare earth elements geochemistry and genesis of the Keban-West Euphrates (Cu-Mo)-Pb-Zn skarn deposit (Eastern Taurus metallogenic belt, E Turkey). *Ore Geol. Rev.* **2019**, *114*, 103102. [[CrossRef](#)]
24. de Siqueira Corrêa, R.; Oliveira, C.G.; Dantas, E.L.; Botelho, N.F. Hydrothermal footprint related to regional-scale shear zone-controlled scheelite mineralization, Seridó W-skarn system, northeastern Brazil. *J. S. Am. Earth Sci.* **2020**, *103*, 102755. [[CrossRef](#)]
25. Wen, G.; Zhou, R.J.; Li, J.W.; Chang, J.; Hu, H.; Yan, D.R.; Wei, K.T.; Jin, S.G. Skarn metallogeny through zircon record: An example from the Daye Cu-Au-Fe-Mo district, Eastern China. *Lithos* **2020**, *378*, 105807. [[CrossRef](#)]
26. Yang, Y.L.; Ni, P.; Wang, Q.; Wang, J.Y.; Zhang, X.L. In Situ LA-ICP-MS study of garnets in the Makeng Fe skarn deposit, eastern China: Fluctuating fluid flow, ore-forming conditions and implication for mineral exploration. *Ore Geol. Rev.* **2020**, *126*, 103725. [[CrossRef](#)]
27. Wang, J.P.; Li, X.W.; Ning, W.B.; Kusky, T.; Wang, L.; Polat, A.; Deng, H. Geology of a Neoproterozoic suture: Evidence from the Zunhua ophiolitic mélangé of the Eastern Hebei Province, North China Craton. *GSA Bull.* **2019**, *131*, 1943–1964. [[CrossRef](#)]

28. Qu, K.; Sima, X.; Fan, G.; Li, G.; Shen, G.F.; Chen, H.K.; Liu, X.; Yin, Q.Q.; Li, T.; Wang, Y. Taipingite-(Ce), $(\text{Ce}_7^{3+}, \text{Ca}_2)_{\Sigma 9}\text{Mg}(\text{SiO}_4)_3[\text{SiO}_3(\text{OH})]_4\text{F}_3$, a new mineral from the Taipingzhen REE deposit, North Qinling Orogen, central China. *Geosci. Front.* **2020**, *11*, 2339–2346. [[CrossRef](#)]
29. Wang, X.M.; Jiao, Y.Q.; Du, Y.S.; Ling, W.L.; Wu, L.Q.; Cui, T.; Zhou, Q.; Jin, Z.G.; Lei, Z.Y.; Weng, S.F. REE mobility and Ce anomaly in bauxite deposit of WZD area, Northern Guizhou, China. *J. Geochem. Explor.* **2013**, *133*, 103–117. [[CrossRef](#)]
30. Lee, S.G.; Asahara, Y.; Tanaka, T.; Kim, N.H.; Yi, K.; Masuda, A.; Song, Y.S. La–Ce and Sm–Nd isotopic systematics of early Proterozoic leucogranite with tetrad REE pattern. *Chem. Geol.* **2010**, *276*, 360–373. [[CrossRef](#)]
31. Qu, K.; Sima, X.; Zhou, H.; Xiao, Z.; Tu, J.; Yin, Q.; Liu, X.; Li, J. In situ LA-MC-ICP-MS and ID-TIMS U–Pb ages of bastnäsite-(Ce) and zircon from the Taipingzhen hydrothermal REE deposit: New constraints on the later Paleozoic granite-related U–REE mineralization in the North Qinling Orogen, Central China. *J. Asian Earth Sci.* **2019**, *173*, 352–363. [[CrossRef](#)]
32. Ondrejka, M.; Uher, P.; Pr. Ek, J.; Ozdin, D. Arsenian monazite-(Ce) and xenotime-(Y), REE arsenates and carbonates from the Tisovec-Rejkovo rhyolite, Western Carpathians, Slovakia: Composition and substitutions in the (REE, Y) XO_4 system (X = P, As, Si, Nb, S). *Lithos* **2007**, *95*, 116–129. [[CrossRef](#)]
33. Taylor, S.R.; McLennan, S.M. The continental crust: Its composition and evolution. *J. Geol.* **1985**, *94*, 57–72.
34. Wang, Q.; Zhao, Z.H.; Xu, J.F.; Bai, Z.H.; Wang, J.X.; Liu, C.X. The Geochemical characteristics of Tongshankou and Yinzu adakitic intrusive rocks in Southeastern Hubei: (Delamination) lower crustal melting and the genesis of porphyry copper deposit. *Acta Petrol. Sin.* **2004**, *20*, 351–360. (In Chinese with English abstract)
35. Li, J.W.; Zhao, X.F.; Zhou, M.F.; Vasconcelos, P.; Ma, C.Q.; Deng, X.D.; Souza, Z.S.D.; Zhao, Y.X.; Wu, G. Origin of the Tongshankou porphyry–skarn Cu–Mo deposit, eastern Yangtze craton, Eastern China: Geochronological, geochemical, and Sr–Nd–Hf isotopic constraints. *Miner. Depos.* **2008**, *43*, 315–336. [[CrossRef](#)]
36. Raimbault, L.; Baume, A.; Dubru, M.; Benkerrou, C.; Zahm, A. REE fractionation between scheelite and apatite in hydrothermal conditions. *Am. Mineral.* **1993**, *78*, 1275–1285.
37. Kozlik, M.; Raith, J.G. Variscan metagranitoids in the central Tauern Window (Eastern Alps, Austria) and their role in the formation of the Felbertal scheelite deposit. *Lithos* **2017**, *278*, 303–320. [[CrossRef](#)]
38. Kozlik, M.; Raith, J.G.; Gerdes, A. U–Pb, Lu–Hf and trace element characteristics of zircon from the Felbertal scheelite deposit (Austria): New constraints on timing and source of W mineralization. *Chem. Geol.* **2016**, *421*, 112–126. [[CrossRef](#)]
39. Brugger, J.; Maas, R.; Lahaye, Y.; McRae, C.; Ghaderi, M.; Costa, S.; Lambert, D.; Bateman, R.; Prince, K. Origins of Nd–Sr–Pb isotopic variations in single scheelite grains from Archaean gold deposits, Western Australia. *Chem. Geol.* **2002**, *182*, 203–225. [[CrossRef](#)]
40. Li, J.W.; Zhao, X.F.; Zhou, M.F.; Ma, C.Q.; Souza, Z.S.D.; Vasconcelos, P. Late Mesozoic magmatism from the Daye region, eastern China: U–Pb ages, petrogenesis, and geodynamic implications. *Contrib. Mineral. Petrol.* **2009**, *157*, 383–409. [[CrossRef](#)]
41. Silva, M.M.V.G.; Lopes, S.P.; Gomes, E.C. Geochemistry and behavior of REE in stream sediments close to an old Sn–W mine, Ribeira, Northeast Portugal. *Geochemistry* **2014**, *74*, 545–555. [[CrossRef](#)]
42. Ghaderi, M.; Palin, M.J.; Campbell, I.H.; Sylvester, P.J. Rare earth element systematics in scheelite from hydrothermal gold deposits in the Kalgoorlie–Norseman region, Western Australia. *Econ. Geol.* **1999**, *94*, 423–437. [[CrossRef](#)]
43. Nilsson, K.K.; Jensen, B.S.; Carlsen, L. Geochemistry and mineralogy of rare earth elements. *Rev. Mineral.* **1989**, *21*, 72–79.
44. Sun, K.K.; Chen, B. Trace elements and Sr–Nd isotopes of scheelite: Implications for the W–Cu–Mo polymetallic mineralization of the Shimensi deposit, South China. *Am. Mineral.* **2017**, *102*, 1114–1128.
45. Sato, K. Tungsten skarn deposit of the Fujigatani Mine, Southwest Japan. *Econ. Geol.* **1980**, *75*, 1066–1082. [[CrossRef](#)]
46. Brugger, J.; Etschmann, B.; Pownceby, M.; Liu, W.; Grundler, P.; Brewe, D. Oxidation state of europium in scheelite: Tracking fluid–rock interaction in gold deposits. *Chem. Geol.* **2008**, *257*, 26–33. [[CrossRef](#)]
47. Song, G.X.; Qin, K.Z.; Li, G.M.; Evans, N.J.; Chen, L. Scheelite elemental and isotopic signatures: Implications for the genesis of skarn-type W–Mo deposits in the Chizhou Area, Anhui Province, Eastern China. *Am. Mineral.* **2014**, *99*, 303–317. [[CrossRef](#)]
48. Hou, Z.Q.; Yang, Z.M. Environmental porphyry deposits in Chinese mainland: Basic geological characteristics, magmatic hydrothermal systems and metallogenic conceptual models. *Acta Geol. Sin.* **2009**, *83*, 1779–1817. (In Chinese with English abstract)
49. Hou, Z.Q.; Yang, Z.M.; Wang, R.; Zheng, Y.C. Further discussion on mineralization of porphyry Cu–Mo–Au deposit in Chinese mainland. *Earth Sci. Front.* **2020**, *27*, 20–44. (In Chinese with English abstract)
50. Sylvester, P.J. Post-collisional strongly peraluminous granites. *Lithos* **1998**, *45*, 29–44. [[CrossRef](#)]
51. Rapp, R.P.; Shimizu, N.; Norman, M.D.; Applegate, G.S. Reaction between slab-derived melts and peridotite in the mantle wedge: Experimental constraints at 3.8 GPa. *Chem. Geol.* **1999**, *160*, 335–356. [[CrossRef](#)]
52. Sen, C.; Dunn, T. Dehydration melting of a basaltic composition amphibolite at 1.5 and 2.0 GPa: Implications for the origin of adakites. *Contrib. Mineral. Petrol.* **1994**, *117*, 394–409. [[CrossRef](#)]